JGR Oceans

RESEARCH ARTICLE
10.1029/2022JC018968

Key Points:

- The Luzon Undercurrent (LUC) is contributed to and characterized by waters from the Deep North Equatorial Current and Luzon Strait middle-layer outflow, and is locally sustained by baroclinic forcing
- Temporally, the LUC intensity has weak seasonality and significant intra-seasonal variation, with two peaks in May/June and October
- Spatially, the LUC shifts from in-shore to off-shore from early summer to late fall, originating from the interior North Pacific and South China Sea middle layer, respectively

Correspondence to:
J. Gan,
magan@ust.hk

Citation:
Li, J., & Gan, J. (2022). Characteristics and formation of the Luzon Undercurrent in the western North Pacific: Observational study. *Journal of Geophysical Research: Oceans*, *127*, e2022JC018968. https://doi.org/10.1029/2022JC018968

Received 9 JUN 2022
Accepted 12 JUL 2022

Author Contributions:
Conceptualization: Junlu Li, Jianping Gan
Data curation: Junlu Li
Formal analysis: Junlu Li
Funding acquisition: Jianping Gan
Investigation: Junlu Li
Methodology: Junlu Li, Jianping Gan
Project Administration: Jianping Gan
Software: Junlu Li
Supervision: Jianping Gan
Validation: Junlu Li
Visualization: Junlu Li
Writing – original draft: Junlu Li
Writing – review & editing: Jianping Gan

Characteristics and Formation of the Luzon Undercurrent in the Western North Pacific: Observational Study

Junlu Li[1,2] and Jianping Gan[1,2]

[1]Department of Ocean Science and Mathematics, Center for Ocean Research in Hong Kong and Macau, The Hong Kong University of Science and Technology, Hong Kong, China, [2]Earth, Ocean and Atmospheric Sciences, The Hong Kong University of Science and Technology (Guangzhou), Guangzhou, China

Abstract The subsurface circulation system in the western North Pacific is dominated by the convergence of the Luzon Undercurrent (LUC) and the Mindanao Undercurrent, which forms the basin-scale eastward North Equatorial Undercurrent jets. The southward LUC, situated to the east of Luzon Island, plays a significant role in transporting subsurface waters equatorward in the western boundary of the subtropical North Pacific. Despite its crucial contributions to the water, heat, and energy distributions in the subsurface layer, its characteristics and formation mechanism remain unclear. In this study, we utilize monthly climatological temperature and salinity data and the derived geostrophic velocity to investigate the spatiotemporal variability of the LUC and its formation dynamics. The LUC transport exhibits weak seasonality and strong intra-seasonal variation, peaking in May/June and October. The origin of the LUC is closely connected with the southward veering of the Deep North Equatorial Current (DNEC) off the Ryukyu Islands and the Luzon Strait middle-layer outflow (LSMO). The DNEC dominates transport in the LUC, and the LSMO of the South China Sea (SCS) Intermediate Water contributes to the water mixing in the LUC. Locally, the appearance of the LUC is dynamically linked with the barotropic effect associated with the sea surface height gradient and the baroclinic effect raised from the downward tilting of the zonal isopycnal off the Philippine coast. Spatially, the core of the LUC shifts from in-shore to off-shore waters from May/June to October. This study reveals the spatiotemporal characteristics of the LUC and identifies its separate origins from the interior North Pacific and the SCS middle layer.

Plain Language Summary In the tropical western North Pacific, the North Equatorial Current bifurcates at the Philippines east coast into two western boundary currents, Kuroshio and Mindanao Current, in the upper ~500 m water depth. This circulation distributes the subtropical water meridionally and plays a significant role in the global ocean circulation and climate change. Below the upper layer circulation, the undercurrent system in 500–1,500 m is critical to the subsurface volume, heat, and salt transport in this region. Among them, the Luzon Undercurrent (LUC) is the most important pathway of the southward subsurface water in the western boundary of the tropical North Pacific. LUC has been widely investigated in the previous studies. However, due to the limitation in the resolution and coverage of the observation data, the characteristics of the LUC and its origins have not been clearly revealed. This study investigates the origins, spatiotemporal variability of the LUC, and its inter-connection with the adjacent subsurface currents. We clarified the spatiotemporal variation of the LUC and its physical linkage with adjacent marginal sea and open ocean. We demonstrated the origins of the LUC in different periods in a year and provided a dynamic interpretation for the formation mechanism of the LUC.

1. Introduction

In the western North Pacific (WNP), the North Equatorial Current (NEC) bifurcates into the northward Kuroshio Current (KC) and southward Mindanao Current (MC), forming the NEC-KC-MC (NKM) circulation system near the east coast of the Philippines (black arrows in Figure 1) (Hu et al., 2020; Kashino et al., 2009; Nitani, 1972; Qiu & Lukas, 1996; Qu et al., 1998; Toole et al., 1990; Zhai et al., 2014). The KC and MC are strong and narrow western boundary currents, which are crucial to the freshwater/heat/energy transport and dynamic interaction between the Pacific and neighboring marginal seas (i.e., the South China Sea (SCS) and the East China Sea) (Chern et al., 1990; Gan et al., 2016; Guo et al., 2006; Kashino et al., 1999; Nan et al., 2015). Below the NKM circulation, an undercurrent system (NKMU), including the North Equatorial Undercurrent (NEUC), the Luzon Undercurrent (LUC), and the Mindanao Undercurrent (MUC), has been reported in recent years (white dashed arrows in Figure 1). The important role of these currents in the North Pacific intermediate water distributions

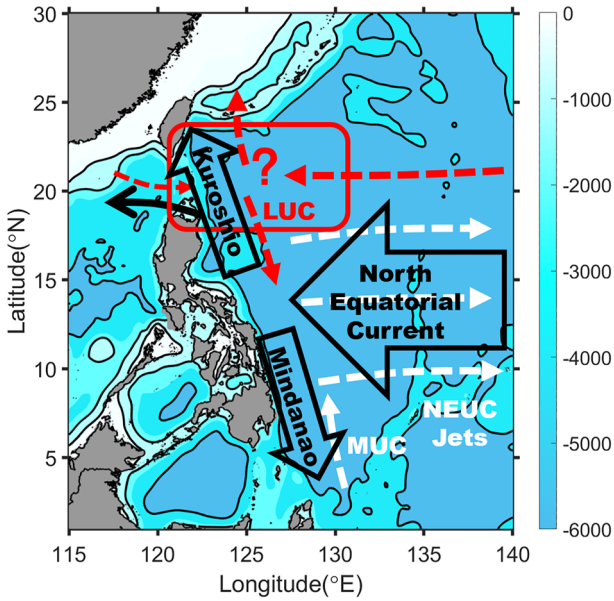

Figure 1. Bathymetry (m) and schematic of the main upper-layer currents (black arrows) and middle-layer undercurrent system (dashed arrows) in the western North Pacific (WNP). The upper-layer currents are the North Equatorial Current, the Kuroshio Current and the Mindanao Current. Below the upper layer, the Luzon Undercurrent (LUC) and Mindanao Undercurrent (MUC) converge to form the North Equatorial Undercurrent (NEUC) jets. The red dashed arrows and the red box indicate the previously unclear subsurface flows and the focused region of this study, respectively.

has been widely studied (Hu & Cui, 1989; Hu et al., 1991, 2013; Li & Gan, 2020; Lien et al., 2015; Qu et al., 1997, 2012; Ren et al., 2018; Schönau & Rudnick, 2017; Wang et al., 2015; Zhang et al., 2017).

The western boundary undercurrents (LUC and MUC) converge below the upper layer NKM circulation system and feed into the eastward NEUC jets (Li & Gan, 2020; Wang et al., 2015). According to Li and Gan (2020), the LUC and MUC contribute to the northern and southern parts of the NEUC, and the LUC serves as a major pathway for the equatorward transport of subsurface water. At the beginning of the 1990s, the existence and characteristics of the LUC were revealed for the first time from the hydrographic data collected by cruises (Hu & Cui, 1989). The LUC is located beneath the KC (Figure 1), with a maximum geostrophic velocity of 0.03–0.07 m s^{-1} and geostrophic transport of 2–4 Sverdrup (Sv) (Hu & Cui, 1989; Qu et al., 1997; Wang et al., 2015). In recent years, automatic glider and moored acoustic Doppler current profiler (ADCP) observations have found that the LUC has exhibited an annual mean velocity core of >0.1 m s^{-1} since 2010 (Chen et al., 2015; Hu et al., 2013; Lien et al., 2015). With the advancement of high-temporal-resolution ADCP measurements, strong intra-seasonal signals of the LUC, caused by subthermocline eddies, have been identified (Wang et al., 2014). However, the limited temporal and spatial resolution of observations obscures the origins, characteristics, formation processes, and variabilities of the LUC in the complex current system of the WNP.

Numerical ocean modeling has been used to investigate the LUC. Gao et al. (2012) studied the origin and pathway of the LUC and found that most of the LUC water originates from the subtropical North Pacific, with 41% of the tracers coming from the Kuroshio extension. Wang and Hu (2012) suggested that the LUC could be traced back to the confluence region of the KC and Oyashio. These studies all used the water property tracking approach. However, investigation of the link between the LUC and the time-dependent, three-dimensional circulation in the WNP, which is crucial to developing a holistic understanding of the LUC, has not been conducted. Furthermore, the subsurface interconnection of the LUC with the adjacent marginal SCS, which proved to be important to the LUC in this study, has not been investigated.

The LUC at ~18°N links with both the deep NEC (DNEC) at ~18–23°N and the Luzon Strait middle-layer outflow (LSMO) (Gan et al., 2016; Tian et al., 2006; Yang et al., 2010; Zhang et al., 2015). The LSMO transports 1–5 Sv at a depth of ~500–1,500 m, with the outflow expected to feed the subsurface LUC. In the eastern side of the LUC, the NEC at 135°–140°E deepens northward, reaching ~1,500 m at 18°–25°N (Qiu et al., 2013; Zhai et al., 2013), and forming the DNEC. This westward current reaches Taiwan Island and the sea mountains in the Luzon Strait (LS), then bifurcates into northward and southward branches. The northward branch directly flows into the deep KC (DKC) below the upper layer KC to the east of Taiwan. Thus, the KC becomes deeper and stronger after passing Taiwan. The southern branch of the DNEC is believed to converge with the LSMO, and both contribute to the origin of the LUC (red dashed arrows in Figure 1). The variability of the LUC is sensitive to the characteristics of the subsurface circulation within the focused region (red box in Figure 1), which still remains largely unclear. This study investigates the physical spatiotemporal interconnections between the LUC and adjacent subsurface currents (i.e., LSMO, DNEC, and DKC).

2. Data and Methods

We utilized a historical three-dimensional hydrographic data set to conduct our investigation. The subsurface temperature and salinity data were obtained from the World Ocean Atlas 2013 (WOA13), which is a long-term objectively analyzed climatological data set provided by the National Oceanic and Atmospheric Administration (Locarnini et al., 2013; Zweng et al., 2013). WOA13 has been widely used to depict the geostrophic current

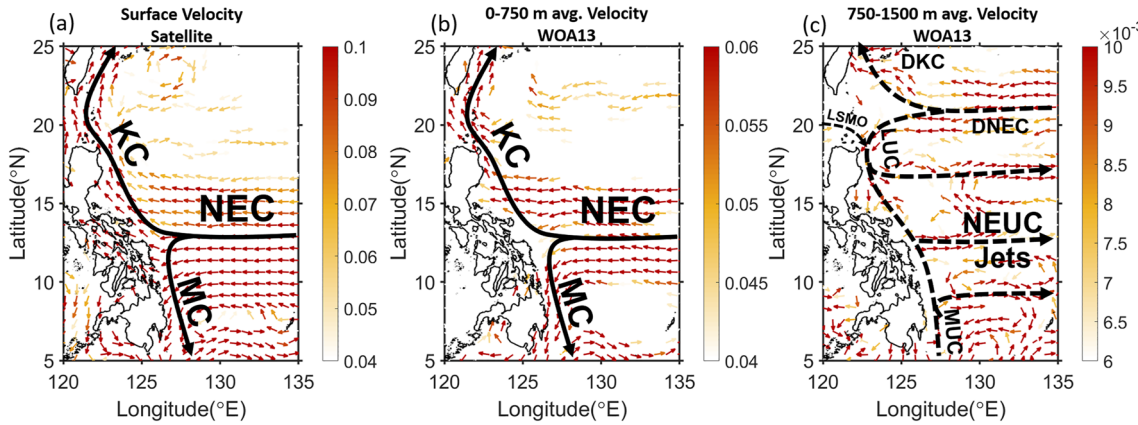

Figure 2. Annual mean (a) surface velocity (m s^{-1}) derived from satellite altimetry data, (b) geostrophic velocity (m s^{-1}) averaged over 0–750 m and (c) geostrophic velocity (m s^{-1}) averaged over 750–1,500 m. The geostrophic velocities are derived from the temperature and salinity of Word Ocean Atlas 2013 (WOA13) data based on thermal wind relation. Solid arrows indicate surface currents of the NEC, KC and MC in (a) and (b). Dashed arrows indicate undercurrents of the NEUC Jets, LUC, MUC, deep KC (DKC), deep NEC (DNEC), and Luzon Strait middle-layer outflow (LSMO) in (c).

globally (Qu & Lukas, 2003; Wang et al., 2019; Zhang & Thomas, 2021). We used the climatological monthly data averaged from 2005 to 2012 with the spatial resolution of 0.25° × 0.25°.

Based on the thermal wind relation, we calculated the geostrophic velocity in the water column from the temperature and salinity, with a reference depth set at 1,500 m. According to previous studies, the speed of water motion decreases rapidly below 1,200 m (Qu et al., 1999) and the difference in geostrophic velocities in the WNP calculated by different reference depths (i.e., 1,500, 2,000, and 2,500 m) is small (Qu et al., 1998). The reference depths of 1,200 m–1,500 m have been widely used in previous studies (Qu & Lukas, 2003; Wang et al., 2015).

For the upper layer circulation, we adopted the surface absolute geostrophic velocity derived from the absolute dynamic height estimated by optimal interpolation, merging the measurements from multiple altimeter missions. This product was processed by the Data Unification and Altimeter Combination System and provided by the Copernicus Marine Environment Monitoring Service (https://marine.copernicus.eu/). The surface absolute geostrophic velocity data were used to validate the geostrophic velocity calculated from the temperature and salinity obtained from the WOA13. This satellite altimetry product also provides the sea surface height (SSH) anomaly data for further analysis. For consistency and validation, we used climatological monthly satellite data and WOA13 data from 2005 to 2012.

3. Results

3.1. Characteristics of the LUC and Its Interconnections With Undercurrents

At the sea surface, the westward NEC is located from ~8° to 18°N in the WNP and bifurcates at ~13°N into the northward KC and southward MC, according to the absolute geostrophic velocities obtained from satellite data (Figure 2a). In the upper layer, averaged from 0 to 750 m, the circulation, derived from the geostrophic velocity, exhibits the spatial pattern of the NKM (Figure 2b). Below the upper layer, averaged from 750 to 1,500 m, the NKMU system is characterized by the NEUC jets, the LUC, and the MUC (Figure 2c). The LUC and MUC of the two western boundary undercurrents converge along the east coast of the Philippines and form three independent eastward NEUC jets, located at 9°, 13°, and 18°N. The location, intensity, and width of the NEUC jets are consistent with previous studies (Qiu et al., 2013). The subsurface velocity patterns provided by the geostrophic velocity are well validated. Unlike the MUC, which transports equatorial subsurface waters and links with the undercurrents in the southern hemisphere (Qu et al., 2012), the LUC originates from the east side of the LS and is connected with the westward DNEC and eastward LSMO. The DNEC is clearly bounded by the northernmost eastward NEUC jet at 18°N and reaches north of 23°N. Similar to the NEC bifurcating at 13°N in the upper layer, the westward DNEC bifurcates and forms the northward and southward branches at ~21°N to the east of the LS. The southern branch feeds into the LUC and the northern branch of the DNEC contributes to the northward subsurface flow of the DKC east of Taiwan. Meanwhile, the LSMO sourced from the middle layer of the SCS

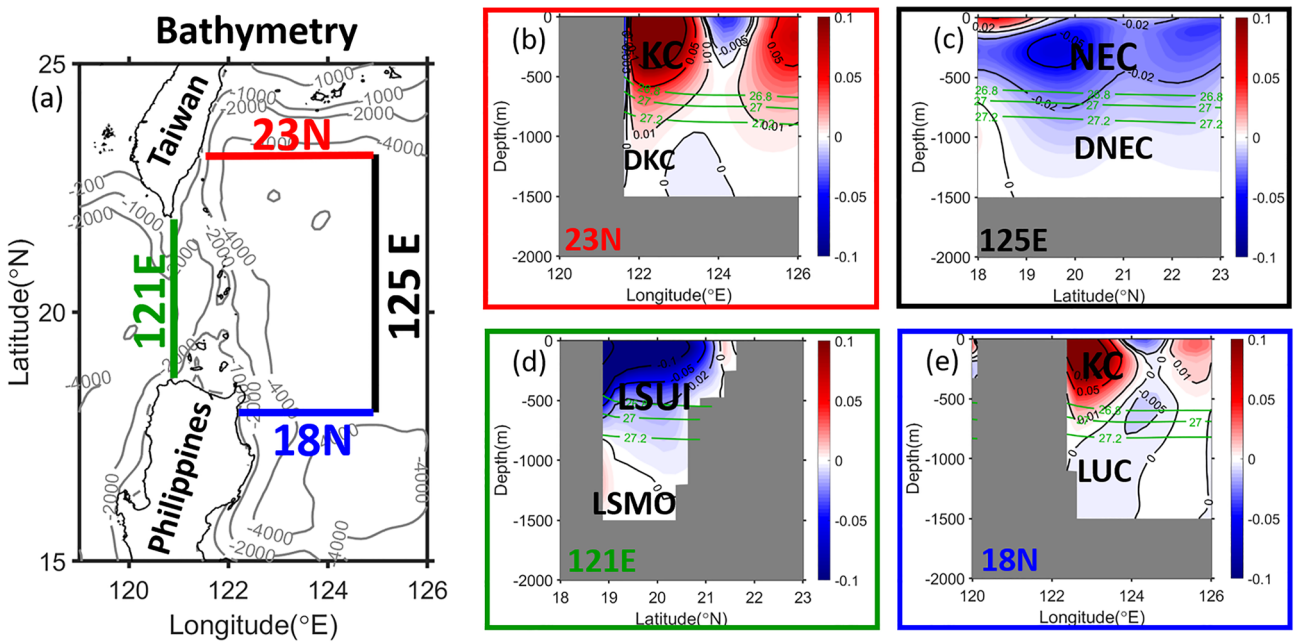

Figure 3. (a) Bathymetry (m) near the Luzon Strait (LS) and annual mean cross-section geostrophic velocity (m s^{-1}) at (b) 23°N, (c) 125°E, (d) 121°E and (e) 18°N. Positive values indicate northward velocities in (b) and (e), and eastward velocities in (c) and (d). The KC, DKC, NEC, DNEC, LUC, LSMO, and LS upper-layer inflow (LSUI) are indicated.

passes through the southern part of the LS and contributes to the LUC. The horizontal velocity field in the middle layer exhibits the connections among the LUC, DNEC, LSMO, and DKC. The spatial pattern of the subsurface circulation in the WNP and SCS provides formation evidence of the LUC.

We focused on the region bounded by 18°N, 23°N, 121°E, and 125°E (Figure 3a) to investigate the LUC. These specific longitudes/latitudes are chosen because the topography and coastline along these sections are not largely affecting the circulation, and they are widely used in previous studies. The KC and LUC structures are shown by velocities normal to the section 18°N from the Philippine coast to 125°E (Figure 3e). A major part of the KC is trapped ~200 km off the coast and above the isopycnal of the potential density $\sigma_\theta = 27.2$ kg m^{-3}. Below this isopycnal, the LUC flowing opposite to the KC extends from the bottom of the KC to a depth greater than 1,500 m. The velocity profiles along sections 23°N, 125°E, and 121°E show the respective upper layer currents and subsurface currents indicated in Figures 3b–3d. The DKC, unlike the LUC, flows northward to the east of Taiwan (Figure 3b). The broad DNEC is an extension in depth of the upper-layer NEC, flowing westward (Figure 3c). Note that the eastward flow in the upper ~200 m in Figure 3c indicates the subtropical counter current (STCC). The LSMO runs southward as intensified discharge out of the SCS from the southern part of the LS (Figure 3d). The upper layer currents and subsurface undercurrents are generally bounded by the isopycnal surface of $\sigma_\theta = 27.2$ kg m^{-3} near 750 m deep (Figures 3b–3e). Thus, we defined a depth of 750 m as the upper boundary of the undercurrent system in the WNP. The topography shown in Figure 3a indicates a steep slope situated at the east side of the LS, which deepens from ~1,000 m in the middle of the LS to >4,000 m in the Philippine Sea. This ridge blocks a large portion of the DNEC from entering the SCS through the LS, which leads to its bifurcation into the DKC and LUC.

3.2. Spatiotemporal Variability of the LUC

3.2.1. Seasonal Variation and Spatial Patterns

In this study, the four seasons are defined as spring (March, April, May), summer (June, July, August), autumn (September, October, November), and winter (December, January, February). Owing to seasonal variation of the KC/LUC along the 18°N section, the KC is weaker in autumn than in the other three seasons (Figure 4c). However, the intensity of the LUC shows less obvious seasonality. According to previous studies, an intra-seasonal signal

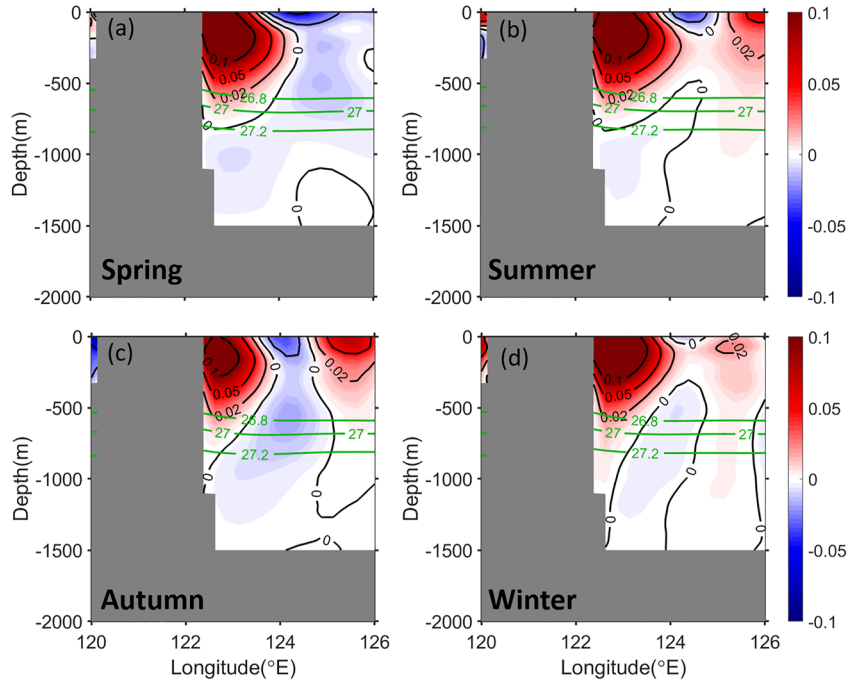

Figure 4. Seasonally mean cross-section geostrophic velocity (m s^{-1}) at 18°N in (a) spring, (b) summer, (c) autumn and (d) winter. Positive values indicate northward velocities. Green contour lines indicate the isopynals of potential density (kg m^{-3}) near the interface between the KC and LUC.

with a period of ~70 days dominates the variation of the LUC intensity (Hu et al., 2013), which is smoothed and removed in the seasonal (90-day) mean results presented in Figure 4. Lien et al. (2015) showed the one-year cycle of the LUC transport from 2012 to 2013, finding a slightly stronger LUC in autumn and a slightly weaker LUC in winter. However, despite the weak seasonality in its transport and intensity, the spatial pattern of the LUC is distinctly seasonal. In spring and summer, the velocity core of the LUC is in-shore (Figures 4a and 4b), while in autumn and winter it moves off-shore and is situated at a shallower depth (Figures 4c and 4d).

As illustrated in Figure 2c, both the DNEC and LSMO are two potential sources of the LUC. The LSMO exhibits more significant seasonal variation, and Figure 5a shows a stable westward transport in the upper layer, but with an intermittent eastward transport in the middle layer across the LS at 121°E in all four seasons. In spring and winter the surface intrusion is strong and the LSMO is weak, whereas in summer and autumn the surface intrusion is weak and the LSMO is strong (Figure 5a). The upper- and middle-layer volume fluxes vary with the same seasonal phase. This suggests that the seasonality of the water flux across the LS may be dominated by the barotropic effect because the barotropic forcing induced by the SSH anomaly gradient has a depth-independent effect applied to the whole water column. The vertical shear of the water flux at 200–300 m is strong in winter and weak in summer. In the upper layer, the meridional profile of the volume flux is stable throughout the year: the KC water enters the SCS mainly in the southern part of the LS (Figure 5b) and exits the SCS in the northern part. In the middle layer, the meridional profile of the volume flux varies significantly in different seasons (Figure 5c). In spring and winter, the westward flux in the middle layer occupies most part of the LS (green and blue lines in Figure 5c). In summer and autumn, the eastward flux exists in the southern part of the LS, whereas the westward flux is trapped in the northern part of the LS (red and yellow lines in Figure 5c). The LSMO is expected to feed into the LUC because it flows eastward through the southern part of the LS, which is geographically linked with the in-shore part of the LUC at 18°N near the northeastern corner of Luzon Island.

The seasonal volume fluxes of the DNEC, DKC, and LUC across the eastern section at 125°E, the northern section at 23°N, and the southern section at 18°N in summer and winter are presented in Figure 6. Due to the spatial resolution of the data, the volume flux near the coastal water is not resolved and it may lead to unperfect balance in the total volume transport, which, however, does not undermine its illustration on the general circulation and origin of the LUC. The spatial pattern and time series of subsurface fluxes from different sources

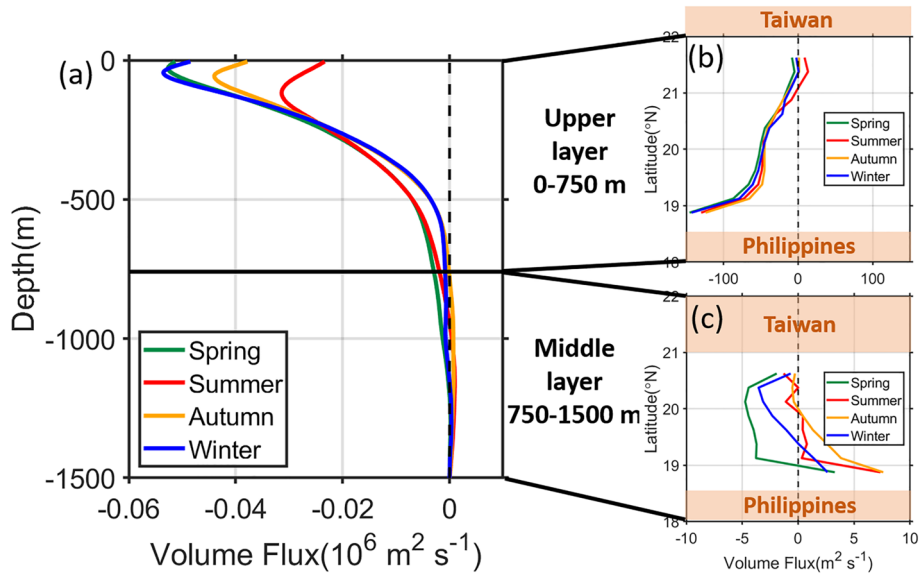

Figure 5. (a) Seasonally mean of the zonal volume flux (10^6 m^2 s^{-1}) meridional-integrated in the LS at 121°E as a function of depth. Seasonally mean of the zonal volume flux (m^2 s^{-1}) integrated over (b) 0–750 m (upper layer) and (c) 750–1,500 m (middle layer) as a function of latitude. Positive values indicate eastward volume fluxes.

provide coherent evidence for the formation of the LUC. The volume flux profiles in Figure 6 illustrate the interconnections between the LUC and adjacent subsurface currents during different time periods. In summer, the DNEC has two strong flux cores located at 22° and 19.5°N, with each core extracting about half of the total DNEC transport (Figure 6a). The transport of the northern and southern cores spatially contributes to the DKC and LUC, respectively. In winter, the DNEC has a similar total volume flux as in summer, but it is slightly intensified in its southern part (Figure 6b). Therefore, its contribution to the DKC is relatively small, and the DKC is weaker in winter. In summer, the LSMO and half of the DNEC contribute to the LUC (Figure 6a). In winter, the LSMO weakens while the DNEC distributes a larger portion southward to feed the LUC, which makes the LUC flux core move offshore relative to its summer location (Figure 6b). Thus, the LUC volume flux at 18°N remains similar in summer and winter but with different spatial patterns.

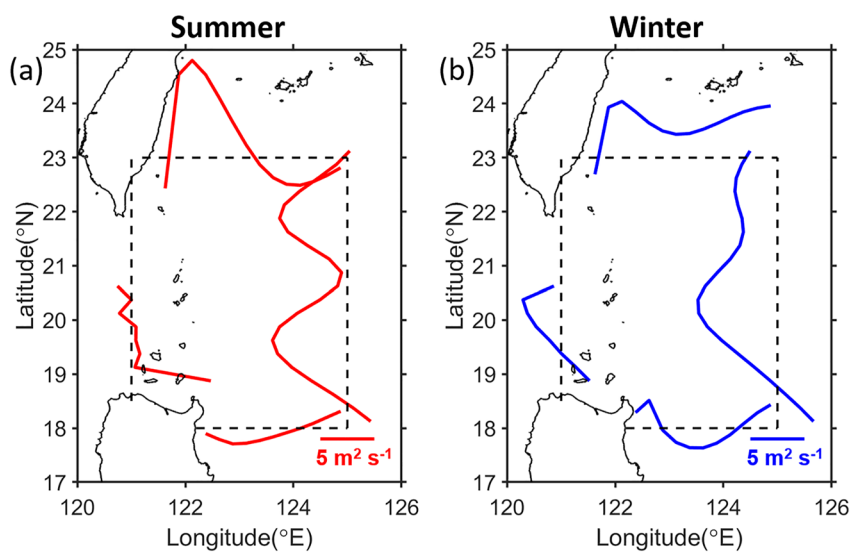

Figure 6. Seasonally mean of the cross-section volume flux (m^2 s^{-1}) integrated over 750–1,500 m at 23°N (north), 125°E (east), 121°E (west), and 18°N (south) in (a) summer (red) and (b) winter (blue). Dashed lines indicate the locations of the four sections and the zero lines of the volume flux profiles.

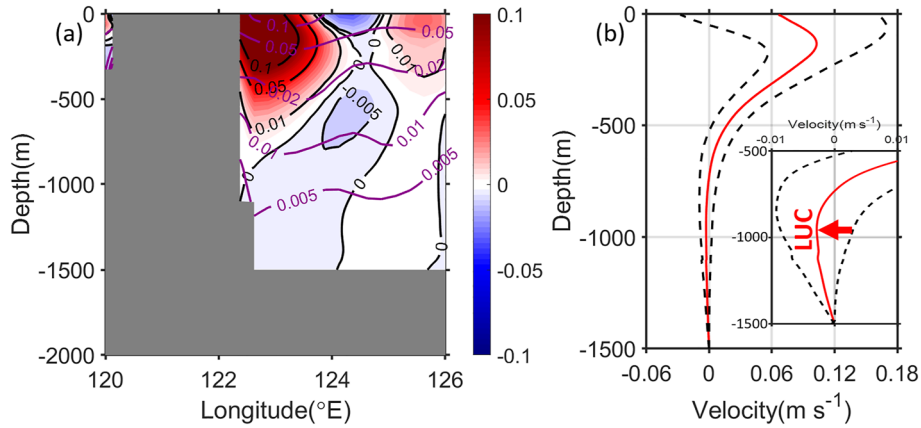

Figure 7. (a) Annual mean of the meridional geostrophic velocity (m s^{-1}, color shading) at 18°N and its standard deviation (purple contour lines). (b) Annual mean of the meridional geostrophic velocity (m s^{-1}, red line) zonal-averaged from the Philippine coast to 125°E along 18°N as a function of depth. Dashed lines in (b) indicate the depth-dependent standard deviation.

3.2.2. Intra-Seasonal Variation

The intra-seasonal variation of the LUC is more significant than the seasonal variation according to high-temporal-resolution moored observations (Hu et al., 2013). The standard deviation (std) of the annual KC is smaller than its mean value (above 750 m in Figure 7a). However, the std is comparable to and larger than the annual mean velocity in the LUC (below 750 m in Figure 7a). Similarly, std is shown to be weaker (greater) than the mean velocity in the upper (middle) layer of the zonal-averaged velocity profile (Figure 7b). Notably, std is slightly stronger than the mean velocity near the sea surface because the southward velocity near 124°E diminishes the mean value. The interface of the upper layer KC and middle layer LUC occurs at ∼750 m, where the mean velocity changes the direction from northward (positive) to southward (negative). The large std below 750 m suggests that the southward LUC exists intermittently, which has also been revealed by the mooring ADCP observations (Hu et al., 2013; Lien et al., 2015).

Thus, to better illustrate the intra-seasonal variation of the LUC and adjacent subsurface currents, we present the monthly downstream volume transport across the focused sections (Figure 8). We only integrate the downstream subsurface transport along each section. The net transport (integrating both positive and negative velocities) exhibits similar variation to the downstream transport (not shown). The LUC transport shows two significant peaks in May/June and October (Figure 8f), which are well correlated with the two peaks of the southward transport derived by data adopted from pressure inverted echo sounders during 2012–2013 (Lien et al., 2015). Lien et al. (2015) also captured the strong LUC transport in May by using sea gliders.

From the monthly transports across the other sections (i.e., 23°N, 121°E, and 125°E), we found that the LUC originates from different sources during different periods. At the eastern boundary along 125°E, we split the DNEC into its southern (DNEC_S) and northern portions (DNEC_N) along the middle latitude of the focused region at 20.5°N (Figures 8d and 8e). Based on the horizontal velocity field shown in Figure 2c, the DNEC_S mainly feeds the southern branch (LUC) while the DNEC_N mainly feeds the northern branch (DKC), after bifurcating along the east side of the ridge in the LS. At the western boundary of the focused region along 121°E, the subsurface flow in the LS is divided into inflow (westward) and outflow (eastward) portions. Corresponding to the meridional profile of the middle-layer volume flux (Figure 5c), the LSMO is situated mainly in the south, and the LS middle-layer inflow (LSMI) is situated mainly in the north (Figures 8b and 8c). Zhang et al. (2015) also observed the LSMI-LSMO structure below 1,000 m along the LS during 2013–2014 by moored observations, as shown in their Figure 4. The LSMO is directly linked to the spatial origin of the LUC.

The two-peak annual cycle of the LUC transport suggests that the intra-seasonal variation is stronger than the seasonal variation in the LUC. In May/June, the LUC reaches its first peak of the year. The DNEC_S provides almost all the transport in the LUC, with a magnitude of ∼1 Sv (Figure 8e). By comparison, the LSMO is weak and makes a limited contribution in these 2 months (Figure 8c). Thus, the LUC transport peak in May/June is

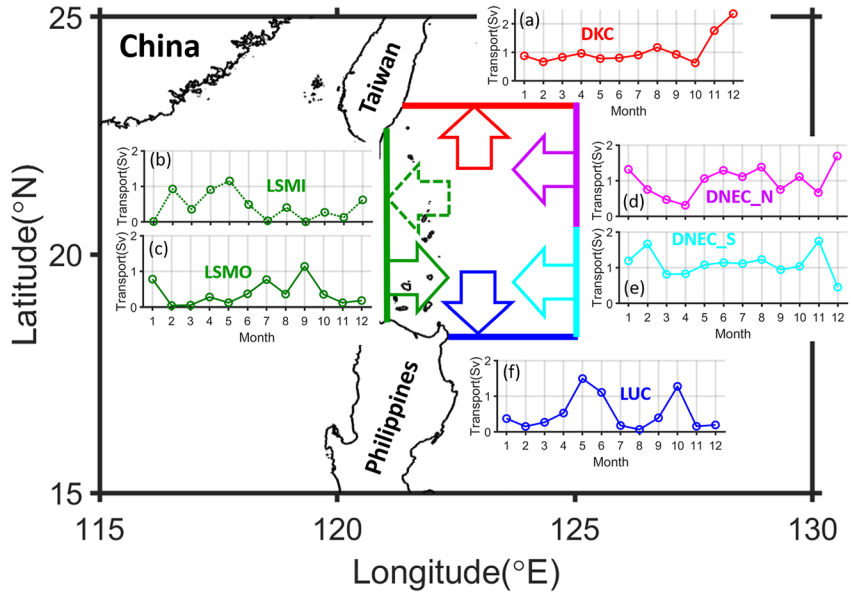

Figure 8. Monthly cross-section downstream volume transport (Sv) integrated over 750–1,500 m at (a) 23°N, (b, c) 121°E, (d, e) 125°E, and (f) 18°N. Arrows indicate the downstream directions of each current.

mainly contributed by the DNEC_S, with only minor modulation by the LSMO. In autumn, the LUC reaches its second peak of the year. Note that the DNEC_S and LSMO transports are comparable in September (Figures 8c and 8e), and they contribute similar volumes of water to the LUC. At the northern boundary (23°N), the DKC is mainly fed by the DNEC_N throughout the year, due to their similar volume transport and variations (Figures 8a and 8d). The volume transports crossing the sections are undoubtedly interconnected and reflect the pathways of the waters related to the LUC. The volume transport is not well conserved in all sections because of the low resolution of near-coast data in the WOA13 data set. In addition, the contribution from the water crossing interface at 750 m is omitted due to the weak vertical motion relative to the horizontal motion.

3.3. Formation and Origin of the LUC

3.3.1. Local Barotropic and Baroclinic Dynamics

In the previous sections, we have shown that the LUC appears and strengthens during May/June and October, and weakens during other months. In addition to the remote influx contributions, the LUC is also sustained by local dynamic conditions. Figure 9 shows the velocity profiles in May and August, which represent the periods with and without the LUC, respectively. In May, the northward KC is weak, and the southward LUC is significantly strong, located just below the KC (Figure 9a). In August, the southward LUC does not exist (Figure 9b), that is, the velocity below the strong KC is weaker but remains northward. The local dynamics that sustain the existence of the LUC is the zonal density gradient. Within the upper layer, the isopycnals' tilting sustains the northward KC during May and August (Figures 9c and 9d). This current is baroclinically responsive to the barotropic effect induced by the zonal SSH anomaly gradient (not shown here). Below the KC, the isopycnals within the LUC depth (i.e., 750–1,500 m) tilt oppositely in May and August. When the LUC is strong (i.e., in May), the isopycnals below the upper layer, such as the potential density $\sigma_\theta = 27.5\,\mathrm{kg\,m^{-3}}$ isopycnal, tilt significantly downward when approaching the coast (Figure 9c). This tilting provides a positive zonal density gradient to drive a southward velocity anomaly, according to the thermal wind relation. In contrast, the isopycnals below 750 m tilt upward toward the coast during August (Figure 9d). Thus, the dynamic condition in the period without the LUC is favorable for a northward velocity, consistent with the northward subsurface current below the KC shown in Figure 9b. The correlation of the LUC and the density field reflects the importance of the baroclinic effect as a dynamic sustaining the variability and existence of the LUC.

We compared the different dynamics during the periods with and without the LUC in the previous paragraph. In addition to those dynamic variations, the LUC in May/June and October also exhibits unique patterns and specific

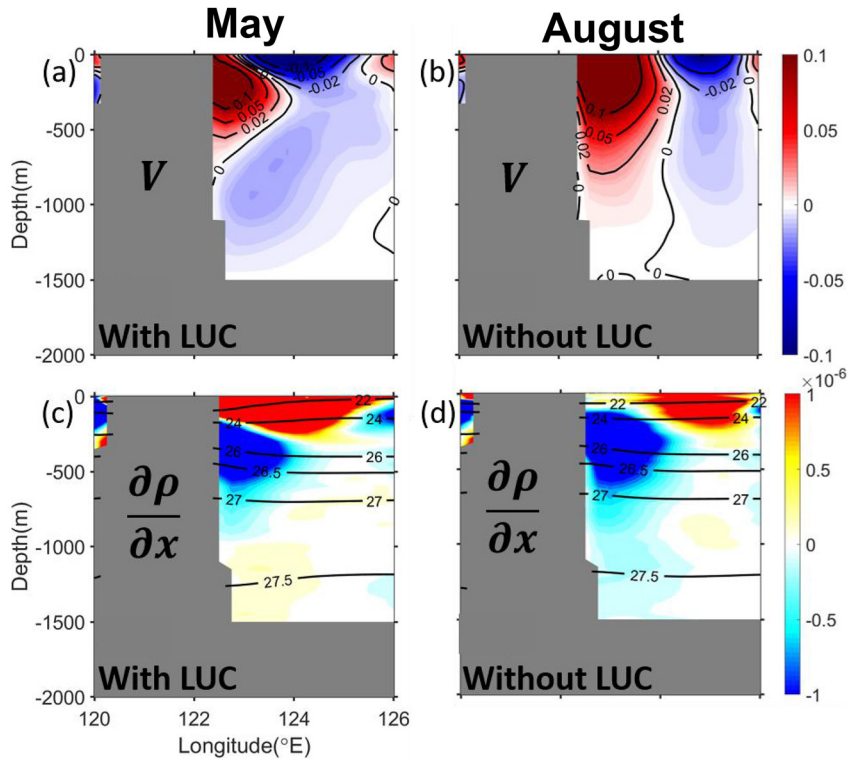

Figure 9. Monthly mean of the meridional geostrophic velocity (m s^{-1}) in (a) May and (b) August at the section of 18°N. Positive values indicate northward velocities. Monthly mean of the potential density (kg m^{-3}, black contour lines) and zonal potential density gradient (kg m^{-4}, color shading) in (c) May and (d) August at the section of 18°N.

underlying formation mechanisms. Figure 10a shows the monthly variation of the depth-averaged velocity at 750–1,500 m between the coast and 126°E along 18°N. The intensity of the LUC in May/June is slightly stronger than that in October (Figures 8f and 10a), and the core of the LUC remains close to the coast. In October, the core moves eastward to ∼124°E (Figure 10a). According to the spatial patterns of the LUC during these two periods, we define the LUC in May/June and October as an in-shore and off-shore LUC, respectively (Figure 10a). During these two periods with specific types of LUC, the vertical profiles of the meridional velocity and velocity shear exhibit unique characteristics. In February and May (red solid and dashed lines in Figure 10c), the intensities in the upper-layer KC are similar. The LUC in May is mainly caused by the strong vertical shear of the velocity at the depth of 300–500 m (Figures 10c and 10d). Thus, the vertical shear of the meridional velocity induced by the strong zonal density gradient generates the southward LUC in May/June. In October, strengthening of the LUC correlates simultaneously with weakening of the KC. This southward velocity anomaly in the whole water column reflects the barotropic effect caused by the SSH anomaly gradient. Using satellite remote sensing data, we found that the zonal SSH difference $\frac{\Delta \eta}{\Delta x}$ between the coast and 125°E is relatively small when the LUC appears (i.e., in May and October, Figure 10b). When the SSH anomaly difference weakens, the barotropic pressure gradient force (PGF) is offset by the baroclinic effect and provides a sufficient dynamic condition for the formation of a southward velocity in the LUC below the upper layer.

In summary, the formation of LUC can be attributed to both barotropic and baroclinic processes. The barotropic effect is mainly due to the change in zonal SSH anomaly, in which the weakened zonal barotropic PGF is favorable to both the KC and LUC. The baroclinic effect is induced by strong downward tilting isopycnal toward the coast, in which the baroclinic PGF overcomes the barotropic PGF, making the velocity direction turn from the northward to the southward at the bottom of the KC favorable to LUC formation. The LUC appearing in May/June is caused by the combined effect of the weakening barotropic and strengthening baroclinic PGF, while the LUC in October is mainly caused by weakening of the barotropic PGF.

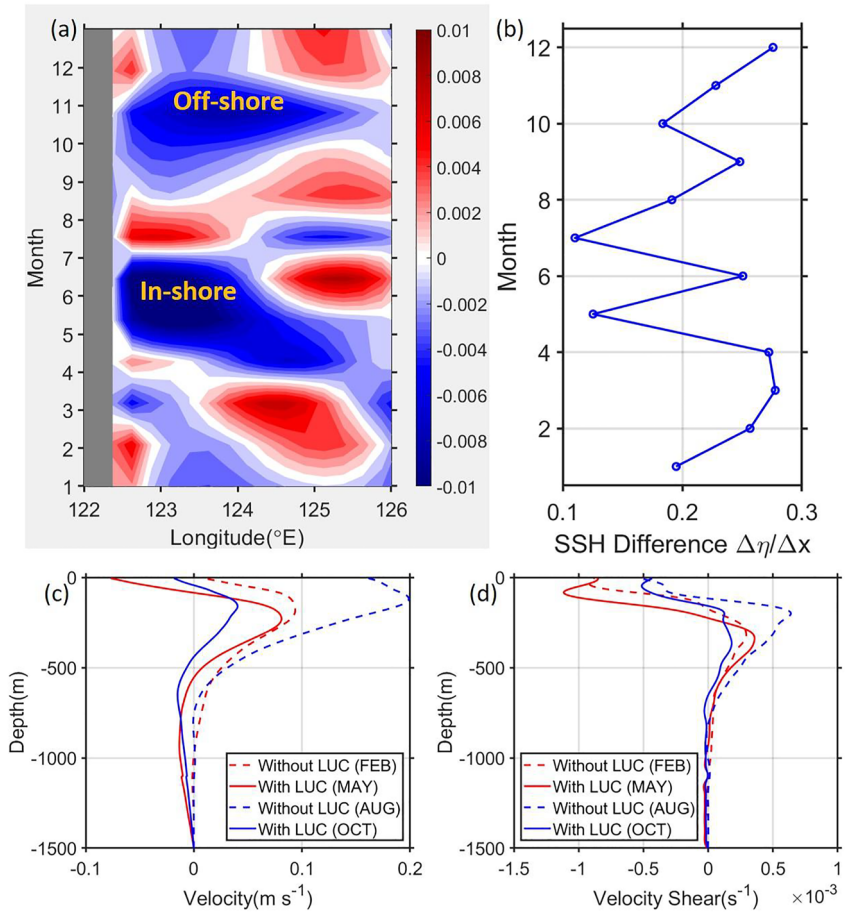

Figure 10. (a) Monthly meridional velocity (m s^{-1}) averaged over 750–1,500 m at the section of 18°N. Positive values indicate northward velocities and negative values indicate the southward LUC. (b) Monthly sea surface height (SSH) anomaly difference $\frac{\Delta\eta}{\Delta x}$ between the Philippine coast and 125°E along the section of 18°N. (c) Monthly mean of the meridional velocity (m s^{-1}) averaged between the Philippine coast and 125°E at 18°N and (d) its vertical shear (s^{-1}) in February, May, August, and October.

3.3.2. Spatiotemporal Origins of LUC

As shown by Figure 10a, the in-shore and off-shore modes of the LUC indicate different origins of the LUC during different periods of a year. We used the empirical orthogonal function (EOF) to investigate the intensity, variation, and the potential origins of the LUC. We took three EOF modes to decompose the signal of the LUC based on the time-dependent velocity section along 18°N from 500 to 1,500 m (Figure 11). The first (EOF1) and second (EOF2) EOF modes contribute 57% and 37% of the variability, respectively. EOF1 exhibits a southward velocity in-shore and a northward velocity off-shore (Figure 11a), and is the main contributor to the in-shore portion of the LUC. In contrast, EOF2 exhibits a southward velocity on the offshore side (Figure 11b) and is the main contributor to the offshore portion of the LUC. The dominant period of EOF2 is ∼3 months which is the typical period of meso-scale eddies. Thus, EOF2 is mainly caused by meso-scale variability. The third EOF mode only contributes 6% and shows a smaller spatial scale than the LUC (Figure 11c), which is likely caused by the processes smaller than meso-scale variability. We therefore focus on the first two EOF modes to reveal the characteristics of the different LUC spatial patterns.

The time series of EOF1, the LUC in-shore mode, is similar to the temporal variation of the LUC transport, peaking in May/June and October (Figures 8f and 11d). The time series of EOF2, the LUC off-shore mode, shows approximately four cycles per year, peaking in January, April, July, and October. For the months (May, June and October) when the LUC is strengthened, we reconstructed the velocity profiles of the LUC as a function of longitude by the EOF modes with their respective time series (Figure 12). The reconstructed LUC velocity

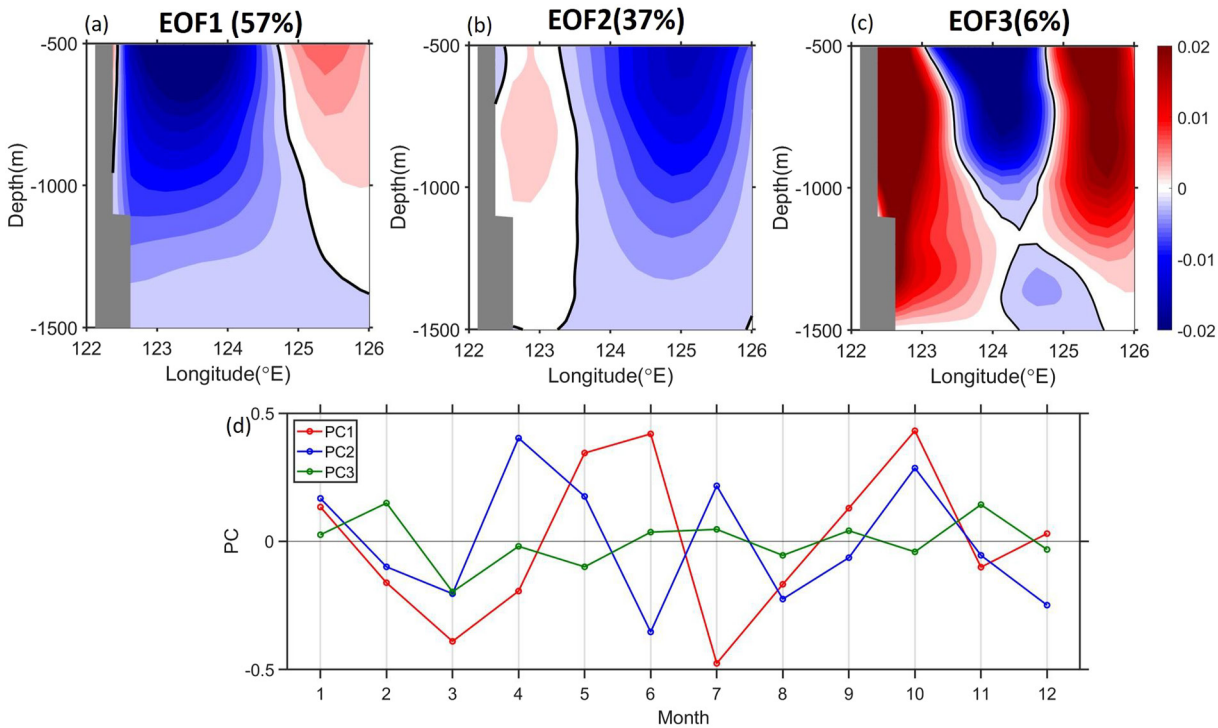

Figure 11. The spatial pattern of the (a) first (EOF1), (b) second (EOF2), and (c) third (EOF3) modes of the EOF analysis at the section of 18°N. EOF1 and EOF2 represent the in-shore and off-shore LUC modes, respectively. (d) Monthly principal components (PC1, PC2, and PC3) represent the time series of the three EOF modes.

profiles (dashed lines in Figure 12) have two distinct patterns. In May, EOF1 and EOF2 are both positive, and EOF1 is stronger than EOF2. Thus, EOF1 dominates the pattern of the LUC profile, which is slightly in-shore (Figure 12a). In June, EOF1 keeps its intensity and sign, whereas EOF2 changes from positive to negative, so that it also contributes to the in-shore pattern. Therefore, the velocity of the LUC remains close to the coast, forming a strongly in-shore LUC (Figure 12b). In October, both EOF1 and EOF2 are positive and comparable. Consequently, the velocity core of the LUC is ~150 km away from the coast because of the combined effects of EOF1 and EOF2, producing an off-shore LUC pattern. The different spatial patterns of the in-shore and off-shore LUCs suggest that the major water masses of the LUC may originate from different sources, such as the subsurface of the SCS and the intermediate North Pacific.

3.3.3. Origins of Water Mass in the LUC

In Figure 8, the LUC origins are identified to be linked mainly with the DNEC in May/June and the LSMO in October. Figure 13 shows that the water masses of the DNEC (i.e., 130°E section, black circles), DKC (i.e., 23°N section, red circles) and LSMO (i.e., 121°E, green circles) are similar during these two periods. The DNEC and DKC contain the North Pacific Intermediate Water (NPIW) with low salinity. The salinity increases with depth and connects with the Arctic Intermediate Water (AIW)/Antarctic Intermediate Water (AAIW) at the bottom. The NPIW originates from the convergence of Kuroshio and Oyashio, and extends southward to the NEC/DNEC region. The AIW and AAIW originate from the Arctic and Antarctic regions, respectively, and they subduct to the bottom of the NPIW. The LSMO extracts the SCS Intermediate Water (SCSIW) because of the inflows in the upper and bottom layer of the LS through interaction between the cross-layer dynamics within the SCS (Cai & Gan, 2020; Gan et al., 2016). The salinity of the LSMO is significantly higher than in the DNEC and DKC (Figure 13). The temperature and salinity characteristics of the LUC water suggest that it originates from a mixture of the DNEC and LSMO waters (Figure 13). In May, the temperature-salinity (T-S) diagram of the LUC water presents characteristics more similar to the DNEC/DKC water than to the LSMO water, indicating that during this period the LUC water mainly originates from the interior of the North Pacific, that is, NPIW/AIW (Figure 13a). In October, the T-S diagram of the LUC water becomes more like that of the LSMO water, which suggests that the LUC is fed by the mixing of the SCSIW and NPIW/AIW/AAIW during this period. The

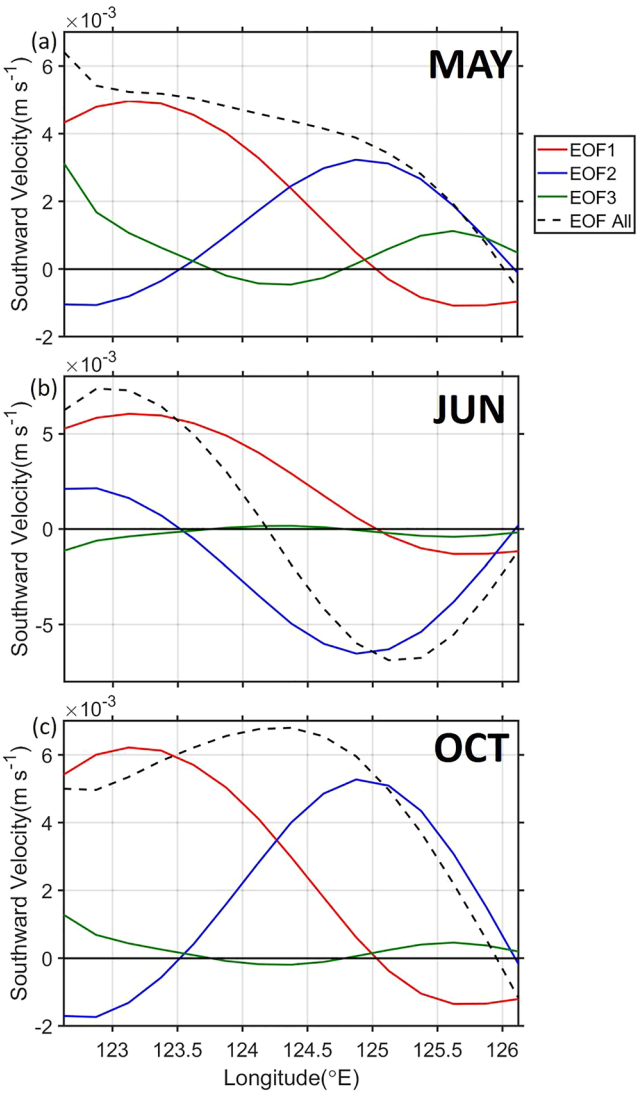

Figure 12. Monthly mean of the meridional velocity (m s^{-1}) averaged over 750–1,500 m of EOF1 (red), EOF2 (blue), EOF3 (green), and total EOF (dashed black lines) in (a) May, (b) June and (c) October.

conclusion based on these water properties is consistent with that according to the volume transport: the LUC originates mainly from the DNEC in May/June and from the convergence of the DNEC and LSMO in October.

To investigate the interconnections among the undercurrents based on temperature and salinity, the temporal variations of the water properties in the relevant subsurface currents are shown in Figure 14. The anomalies of monthly temperature and salinity in the downstream undercurrents (i.e., LUC, DKC, DNEC_N, DNEC_S, and LSMO) at their respective sections (Figure 8) are used to depict the correlation between the LUC and adjacent undercurrents. The temperature and salinity anomalies in the DKC, DNEC_N, DNEC_S, and LUC have limited deviations from the mean values. By contrast, the temperature and salinity in the LSMO deviates significantly from the mean values (strong variability), which suggests that the LSMO and LSMI consist of different water masses. The LSMI contains subsurface North Pacific waters (i.e., NPIW/AAIW/AIW), whereas the LSMO contains subsurface SCS waters (i.e., SCSIW). The SCS intermediate layer has a dramatically lower temperature (Figure 14a) and a higher salinity (Figure 14b) than the Pacific intermediate layer. In Figure 14, the correlations between the LUC and the DKC/DNEC_N/DNEC_S are weak because the DKC/DNEC_N/DNEC_S are almost purely originated from interior North Pacific. Yet, the correlation coefficients (CC) between the LUC (blue) and LSMO (green) are statistically significant for both the temperature and salinity, especially in the second half of the year when the LSMO is strong, as shown in Figure 8c. Their CC for temperature is 0.67 with a confidence level of 99%, while for salinity their CC is 0.56 with a confidence level of 95%. The higher CCs between the LUC and the LSMO than those between the other adjacent undercurrents indicates that the variability of the water properties in the LUC is strongly affected by the SCSIW through the LSMO, although the volume transport of the LSMO is limited. In addition, when the LSMO becomes strong in autumn, the temperature and salinity of the LUC water drift toward the temperature and salinity of the LSMO (Figure 13b). Thus, it is apparent that the water property of the LUC is dominated by the SCSIW through the LSMO.

4. Summary

In the WNP, the undercurrent system NKMU is situated below the upper-layer NKM circulation, in which the LUC is one of the most important western boundary undercurrents, transporting subsurface water southward. The southward LUC converges with the northward MUC to form three NEUC jets carrying subsurface water eastward to the central and eastern North Pacific. This undercurrent system dominates the subsurface water transport and heat/energy distribution in the tropical and subtropical North Pacific, and is linked with the middle layer of the adjacent ocean, that is, the SCS, through the LS (Figure 15). Investigating the spatiotemporal variation and formation dynamics of the LUC is crucial to improving our understanding of the subsurface circulation and water distribution in the WNP.

We utilized the historical hydrographic observational data from the WOA13 data to investigate the spatiotemporal characteristics of the LUC, its interconnection with subsurface currents, the origin and formation dynamics of the LUC. The WOA13, although has a relatively low resolution, has the best spatiotemporal coverages to resolve the LUC. We focused on a region east of the LS: a closed box bounded by the 18°N (east of Luzon Island, LUC), 23°N (east of Taiwan, DKC), 121°E (LS), and 125°E (DNEC) sections(Figure 15). The DNEC bifurcates when approaching the LS, dividing into the northern and southern parts (DNEC_N and DNEC_S). Seasonally, the LUC is relatively strong and is located offshore in autumn. According to the annual mean value, the LSMO exists south of the LS while the LSMI is in the north. Generally, in the annual to seasonal timescale, the LSMO converges

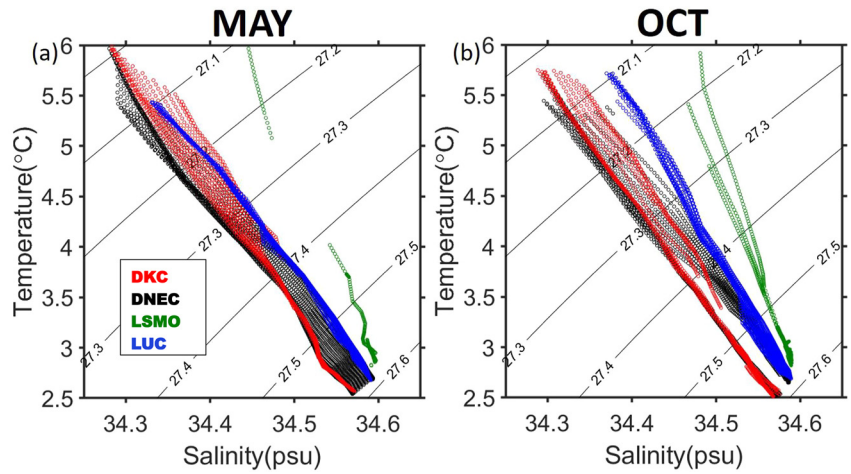

Figure 13. Monthly mean of the T-S diagram of the water column in 750–1,500 m at the four focused sections in (a) May and (b) October, see Figure 3a for the representative color of each section.

with the DNEC_S to feed the LUC at 18°N directly, while at the northern boundary of the region, the DKC along 23°N is almost totally contributed by the DNEC_N.

Corroborated by previous ADCP data, we found that the LUC exhibited stronger intra-seasonal than seasonal variability. Specifically, two distinct peaks occurred for the LUC transports in May/June and October. This semi-annual signal of the LUC transport is caused by the two origins of the LUC, that is, the DNEC_S and the LSMO. The DNEC_S transport is stronger than the LSMO transport and contributes to the volume transport of

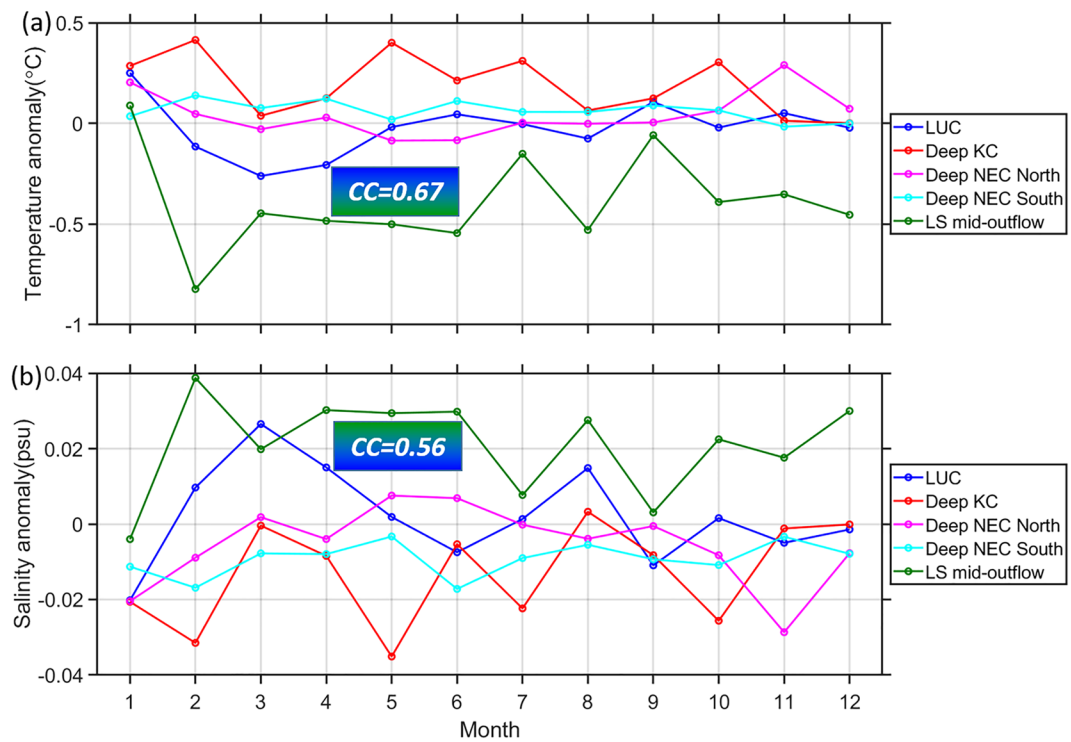

Figure 14. Monthly (a) Temperature (°C) and (b) salinity (psu) averaged in the cross-section downstream velocity areas anomalous to those averaged in the whole area at the sections defined in Figure 8: LUC section at 18°N (blue), DKC section at 23°N (red), DNEC_N section at 125°E from 20.5°N to 23°N (magenta), DNEC_S section at 125°E from 18°N to 20.5°N (cyan), and LSMO section at 121°E (eastward velocity only, green). The Correlation Coefficients (CCs) between the LUC and LSMO waters of the temperature/salinity anomalies are shown.

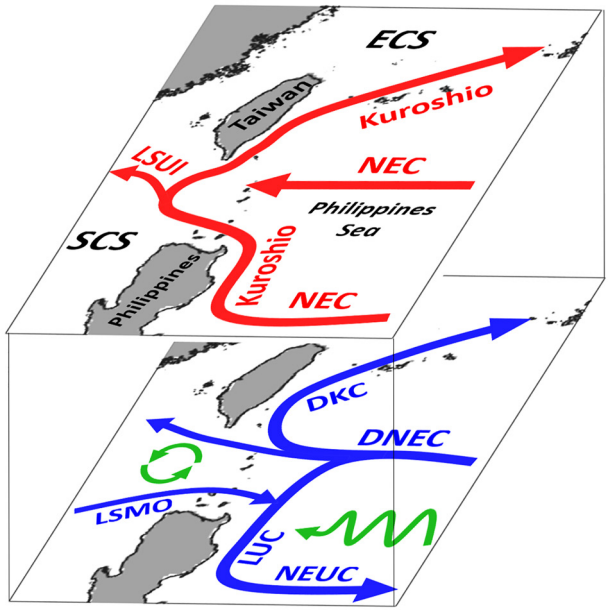

Figure 15. Schematic of the upper-layer (red arrows) and middle-layer (blue arrows) circulation in the WNP and the main currents of concern in this study.

the LUC in both May/June and October. The LSMO strengthens in the second half of the year, and thus mainly contributes to the LUC and its temperature and salinity in October.

The strong LUC peaks in May/June and October have different origins and exhibit unique formation dynamics and spatial patterns. In May/June, the combined strengthened baroclinic effect and weakened baroclinic effect drive the LUC. In contrast, only weakening barotropic effect sustains the LUC in October. We also found an inshore and offshore patterns of the LUC in May/June and October, respectively. EOF analysis provides the spatio-temporal pattern of the LUC during these two periods. The EOF1 mode is an inshore mode, which contributes 57% of the total LUC variability and dominates the LUC pattern in May/June. The EOF2 mode is an offshore mode, which contributes 37% and becomes important in October. The time series of EOF1 shows a similar seasonal phase to the LUC transport, which indicates its relationship with the barotropic/baroclinic dynamics. EOF2 has a higher frequency (~4 cycles per year) than EOF1, which may be caused by meso-scale processes in the LUC with a period of 70–80 days (Hu et al., 2013).

The different sources of the LUC during May/June and October characterize the water properties of the LUC. In May/June, the T-S diagram of the LUC water closely resembles those of the DNEC and DKC waters, while the LUC water becomes significantly saltier and warmer due to influence of the LSMO water in October. In addition, the high correlation of the temperature and salinity anomalies between the LUC and the LSMO suggests that the SCSIW in LSMO strongly affects the variation of the LUC's water properties. Due to the large difference of the water property between the western Pacific Ocean and SCS, small volume of the LSMO can alter temperature and salinity in the LUC significantly. In contrast, although the DNEC contributes a large volume of water to the LUC, their similar temperature and salinity properties limit the effect on changing the LUC water property.

This study revealed the previously unclear features of the subsurface circulation east of the LS in the Philippine Sea and deepened our understanding of the formation dynamics and origins of the LUC.

Data Availability Statement

The data World Ocean Atlas 2013 (WOA13) used in this study can be found at https://climatedataguide.ucar.edu/climate-data/world-ocean-atlas-2013-woa13.

Acknowledgments
This research was supported by the key research project of the National Science Foundation of China (41930539), Center for Ocean Research in Hong Kong and Macau, a joint research center between QNLM and HKUST and the Theme-based Research Scheme (T21-602/16-R, GRF16212720) of the Hong Kong Research Grants Council. We are also grateful for the support of The National Supercomputing Centers of Tianjin and Guangzhou.

References

Cai, Z., & Gan, J. (2020). Dynamics of the cross-layer exchange for the layered circulation in the South China Sea. *Journal of Geophysical Research: Oceans*, *125*(8), e2020JC016131. https://doi.org/10.1029/2020jc016131

Chen, Z., Wu, L., Qiu, B., Li, L., Hu, D., Liu, C., et al. (2015). Strengthening Kuroshio observed at its origin during November 2010 to October 2012. *Journal of Geophysical Research: Oceans*, *120*(4), 2460–2470. https://doi.org/10.1002/2014jc010590

Chern, C. S., Wang, J., & Wang, D. P. (1990). The exchange of Kuroshio and East China Sea shelf water. *Journal of Geophysical Research*, *95*(C9), 16017–16023. https://doi.org/10.1029/jc095ic09p16017

Gan, J., Liu, Z., & Hui, C. R. (2016). A three-layer alternating spinning circulation in the South China Sea. *Journal of Physical Oceanography*, *46*(8), 2309–2315. https://doi.org/10.1175/jpo-d-16-0044.1

Gao, S., Qu, T., & Hu, D. (2012). Origin and pathway of the Luzon Undercurrent identified by a simulated adjoint tracer. *Journal of Geophysical Research: Oceans*, *117*.

Guo, X., Miyazawa, Y., & Yamagata, T. (2006). The Kuroshio onshore intrusion along the shelf break of the East China Sea: The origin of the Tsushima Warm Current. *Journal of Physical Oceanography*, *36*(12), 2205–2231. https://doi.org/10.1175/jpo2976.1

Hu, D., & Cui, M. (1989). *The western boundary current in the far-western Pacific Ocean*. Proceedings of western international meeting and workshop on TOGA COARE. (pp. 123–134). Institut Francais de Recherche Scientifique pour le Dtveloppement en Cooptratlon Noumeéa.

Hu, D., Cui, M., Qu, T., & Li, Y. (1991). *A subsurface northward current off Mindanao identified by dynamic calculation*. Elsevier oceanography series (pp. 359–365). Elsevier.

Hu, D., Hu, S., Wu, L., Li, L., Zhang, L., Diao, X., et al. (2013). Direct measurements of the Luzon Undercurrent. *Journal of Physical Oceanography*, *43*(7), 1417–1425. https://doi.org/10.1175/jpo-d-12-0165.1

Hu, D., Wang, F., Sprintall, J., Wu, L., Riser, S., Cravatte, S., et al. (2020). Review on observational studies of western tropical Pacific Ocean circulation and climate. *Journal of Oceanology Limnology*, *38*(4), 906–929. https://doi.org/10.1007/s00343-020-0240-1

Kashino, Y., España, N., Syamsudin, F., Richards, K. J., Jensen, T., Dutrieux, P., & Ishida, A. (2009). Observations of the North Equatorial current, Mindanao current, and Kuroshio current system during the 2006/07 El Niño and 2007/08 La Niña. *Journal of Oceanography*, *65*(3), 325–333. https://doi.org/10.1007/s10872-009-0030-z

Kashino, Y., Watanabe, H., Herunadi, B., Aoyama, M., & Hartoyo, D. (1999). Current variability at the Pacific entrance of the Indonesian Throughflow. *Journal of Geophysical Research*, *104*(C5), 11021–11035. https://doi.org/10.1029/1999jc900033

Li, J., & Gan, J. (2020). On the formation dynamics of the north equatorial undercurrent. *Journal of Physical Oceanography*, *50*(5), 1399–1415. https://doi.org/10.1175/jpo-d-19-0142.1

Lien, R.-C., Ma, B., Lee, C., Sanford, T., Mensah, V., Centurioni, L., et al. (2015). The Kuroshio and Luzon Undercurrent East of Luzon Island. *Oceanography*, *28*(4), 54–63. https://doi.org/10.5670/oceanog.2015.81

Locarnini, R., Mishonov, A. V., Antonov, J. I., Boyer, T. P., Garcia, H. E., Baranova, A. K., et al. (2013). *World Ocean Atlas 2013, Volume 1: Temperature*. In S. Levitus, & A. Mishonov (Eds.) (Vol. 73, p. 40). NOAA Atlas NESDIS.

Nan, F., Xue, H., & Yu, F. (2015). Kuroshio intrusion into the South China sea: A review. *Progress in Oceanography*, *137*, 314–333. https://doi.org/10.1016/j.pocean.2014.05.012

Nitani, H. (1972). Beginning of the Kuroshio.

Qiu, B., & Lukas, R. (1996). Seasonal and interannual variability of the North Equatorial current, the Mindanao current, and the Kuroshio along the Pacific western boundary. *Journal of Geophysical Research*, *101*(C5), 12315–12330. https://doi.org/10.1029/95jc03204

Qiu, B., Rudnick, D. L., Chen, S., & Kashino, Y. (2013). Quasi-stationary north equatorial undercurrent jets across the tropical North Pacific Ocean. *Geophysical Research Letters*, *40*(10), 2183–2187. https://doi.org/10.1002/grl.50394

Qu, T., Chiang, T. L., Wu, C. R., Dutrieux, P., & Hu, D. (2012). Mindanao Current/Undercurrent in an eddy-resolving GCM. *Journal of Geophysical Research*, *117*(C6). https://doi.org/10.1029/2011jc007838

Qu, T., Kagimoto, T., & Yamagata, T. (1997). A subsurface countercurrent along the East Coast of Luzon. *Deep Sea Research Part I: Oceanographic Research Papers*, *44*(3), 413–423. https://doi.org/10.1016/s0967-0637(96)00121-5

Qu, T., & Lukas, R. (2003). The bifurcation of the North Equatorial current in the Pacific. *Journal of Physical Oceanography*, *33*(1), 5–18. https://doi.org/10.1175/1520-0485(2003)033<0005:tbotne>2.0.co;2

Qu, T., Mitsudera, H., & Yamagata, T. (1998). On the western boundary currents in the Philippine Sea. *Journal of Geophysical Research*, *103*(C4), 7537–7548. https://doi.org/10.1029/98jc00263

Qu, T., Mitsudera, H., & Yamagata, T. (1999). A climatology of the circulation and water mass distribution near the Philippine coast. *Journal of Physical Oceanography*, *29*(7), 1488–1505. https://doi.org/10.1175/1520-0485(1999)029<1488:acotca>2.0.co;2

Ren, Q., Li, Y., Wang, F., Song, L., Liu, C., & Zhai, F. (2018). Seasonality of the Mindanao current/undercurrent system. *Journal of Geophysical Research: Oceans*, *123*(2), 1105–1122. https://doi.org/10.1002/2017jc013474

Schönau, M. C., & Rudnick, D. L. (2017). Mindanao current and undercurrent: Thermohaline structure and transport from repeat glider observations. *Journal of Physical Oceanography*, *47*(8), 2055–2075. https://doi.org/10.1175/jpo-d-16-0274.1

Tian, J., Yang, Q., Liang, X., Xie, L., Hu, D., Wang, F., & Qu, T. (2006). Observation of Luzon strait transport. *Geophysical Research Letters*, *33*(19), L19607. https://doi.org/10.1029/2006gl026272

Toole, J. M., Millard, R. C., Wang, Z., & Pu, S. (1990). Observations of the Pacific North Equatorial current bifurcation at the Philippine coast. *Journal of Physical Oceanography*, *20*(2), 307–318. https://doi.org/10.1175/1520-0485(1990)020<0307:ootpne>2.0.co;2

Wang, F., Wang, Q., Zhang, L., Hu, D., Hu, S., & Feng, J. (2019). Spatial distribution of the seasonal variability of the North Equatorial Current. *Deep Sea Research Part I: Oceanographic Research Papers*, *144*, 63–74. https://doi.org/10.1016/j.dsr.2019.01.001

Wang, F., Zang, N., Li, Y., & Hu, D. (2015). On the subsurface countercurrents in the Philippine Sea. *Journal of Geophysical Research: Oceans*, *120*(1), 131–144. https://doi.org/10.1002/2013jc009690

Wang, Q., & Hu, D. (2012). Origin of the Luzon undercurrent. *Bulletin of Marine Science*, *88*, 51–60.

Wang, Q., Zhai, F., & Hu, D. (2014). Variations of Luzon Undercurrent from observations and numerical model simulations. *Journal of Geophysical Research: Oceans*, *119*(6), 3792–3805. https://doi.org/10.1002/2013jc009694

Yang, Q., Tian, J., & Zhao, W. (2010). Observation of Luzon Strait transport in summer 2007. *Deep Sea Research Part I: Oceanographic Research Papers*, *57*(5), 670–676. https://doi.org/10.1016/j.dsr.2010.02.004

Zhai, F., Hu, D., & Qu, T. (2013). Decadal variations of the North Equatorial current in the Pacific at 137 E. *Journal of Geophysical Research: Oceans*, *118*(10), 4989–5006. https://doi.org/10.1002/jgrc.20391

Zhai, F., Wang, Q., Wang, F., & Hu, D. (2014). Variation of the North Equatorial current, Mindanao current, and Kuroshio current in a high-resolution data assimilation during 2008–2012. *Advances in Atmospheric Sciences*, *31*(6), 1445–1459. https://doi.org/10.1007/s00376-014-3241-1

Zhang, L., Wang, F. J., Wang, Q., Hu, S., Wang, F., & Hu, D. (2017). Structure and variability of the North Equatorial current/Undercurrent from mooring measurements at 130 E in the Western Pacific. *Scientific Reports*, *7*(1), 46310. https://doi.org/10.1038/srep46310

Zhang, R., & Thomas, M. (2021). Horizontal circulation across density surfaces contributes substantially to the long-term mean northern Atlantic Meridional Overturning Circulation. *Communications Earth & Environment*, *2*, 1–12. https://doi.org/10.1038/s43247-021-00182-y

Zhang, Z., Zhao, W., Tian, J., Yang, Q., & Qu, T. (2015). Spatial structure and temporal variability of the zonal flow in the Luzon Strait. *Journal of Geophysical Research: Oceans*, *120*(2), 759–776. https://doi.org/10.1002/2014jc010308

Zweng, M., Reagan, J. R., Antonov, J. I., Locarnini, R. A., Mishonov, A. V., Boyer, T. P., et al. (2013). *World Ocean Atlas 2013, Volume 2: Salinity*. In S. Levitus & A. Mishonov (Eds.) (Vol. 74, p. 39). NOAA Atlas NESDIS.